Thermal features vis a vis strain features of fracturing process in jointed rock layer under concentrated load

Haiqing Yang[1, 2*], Bolong Liu[1, 2], and Shivakumar Karekal[3]

[1]State key laboratory of coal mine disaster dynamics and control, Chongqing University, Chongqing 400045, China.

[2]National Joint Engineering Research Center of Geohazards Prevention in the Reservoir Areas, Chongqing 400045, China.

[3]School of Civil, Mining and Environmental Engineering, University of Wollongong, Wollongong, NSW, Australia 2522.

*Corresponding author: Haiqing Yang (yanghaiqing06@163.com; yanghaiqing@cqu.edu.cn)

†Additional authors: Bolong Liu (20171601009@cqu.edu.cn), Shivakumar Karekal (skarekal@uow.edu.au).

Key points:

- Indention tests were performed on the jointed rock specimens to simulate the fracturing process of jointed layer
- The abnormities in infrared radiation fields and temperature concentration factors in crack initiation processes were appropriately interpreted

- New thermal criteria for two types of crack propagations were proposed.

Abstract

In case of earthquakes and crustal movement, the concentration of impounding load over a large region of crust can cause disturbances to the stratum. In order to quantitatively investigate crack initiation, propagation and coalescence processes of jointed stratum based on thermal variations caused by concentrated mechanical loading, a series of indention tests were performed on granite specimens. In the experiment, fracture process and resulting infrared radiation fields of specimens were respectively recorded by synchronized digital image correlation system and infrared camera. Then, thermal characteristics of mixed shear-tensile and tensile conical crack were analyzed. Experimental results indicate that the highlighted temperature localization is mainly caused by shear deformation within the localized fracture process zone. It is shown that in the initiation process, the abnormities in the temperature concentration factors are caused by the frictional-thermal effect for mixed mode crack and the thermoelastic effect for tensile mode crack. Subsequently, in the propagation process, these two crack types followed newly proposed criteria, namely, the maximum temperature gradient criterion for mixed mode crack and the minimum temperature gradient criterion for tensile mode crack. In addition, the intensity of temperature concentrations in crack initiation stage and coalescence stage are more pronounced than that of crack propagation stage. These thermal effects strongly correlated with the stress states in the cracking process. The new findings from the

infrared radiation temperature distributions improve our understanding of fracturing process of rock mass. Furthermore, it will provide some fundamental references for geophysical prospecting in jointed rock mass.

1 Introduction

Thermal effects are commonly encountered in geological processes, such as neo-tectonic, active fault, earthquakes, landslides and volcanic eruptions. According to the thermal anomalies, the location and characteristics of geological activities can be determined in geophysical prospecting (Lu et al. 2016; Tramutoli et al., 2013; Xiong et al. 2015). In jointed stratum, the concentrated load caused by hills, dam and reservoirs et al. may lead to the fracture of crust, causing the instability of formation and even the secondary disaster, such as reservoir-induced seismicity (Ramasamy et al., 2019; Stiros & Pytharouli, 2018). Consequently, it is pressing to investigate the fracture process in jointed stratum from thermal perspective. As a result, the failure of layer can be detected.

The thermal mechanism of stratum under the loading of tectonic activity has been a longstanding topic in geoscience. For the earthquake, Milne (1886) initially found the temperature changes before large earthquakes. Generally, it is acknowledged that the increase in temperature of a fault mainly caused by shear heating in geoscience (Li et al. 2015). Subsequently, according to the in situ measurements and theories of thermodynamics and heat conduction effect, Chen et al. (2013, 2016) also found that

60 the change in bedrock temperature is accordant with stress adjustment in seismogenic
61 tectonics. Therefore, stress state of bedrock during the earthquake can be detected
62 based on the temperature change. In active fault zone, temperature of the rock varies
63 due to the internal deformation of thrust belts and shear heating under the loading
64 (Bosea & Mukherjee, 2020; Long et al, 2011; Mukherjee, S. 2017). In detail, internal
65 deformation of thrust sheets generally occurs in the forms of layer (or thrust)-parallel
66 simple shear and layer (or thrust)-normal pure shear (Sanderson, 1982), leading to the
67 high temperature. Shear heating is caused by the sliding of one rock unit over the
68 other along fault planes, especially in reverse faulting. Graham and England (1976)
69 initially pointed out that the obvious temperature increase in faulted hangingwall and
70 footwall blocks generally occurs in fault zone with high the slip rate and rock strength.
71 Furthermore, Mukherjee (2017) found that the coefficient of friction, density and
72 thickness of the hangingwall block havelinear correlation with shear heating. Through
73 theoretical investigation on kinematics and shear heat pattern of ductile simple shear
74 zones, Mulchrone1 & Mukherjee (2016) drawn a conclusion that the maximum
75 temperature in shear zones occurs at either boundaries of the shear zone or equidistant
76 from them. However, the thermal characteristics and mechanisms in jointed rock
77 under the concentrated load have scarcely studied in the past.
78 As the temperature can be detected by infrared camera, some scholars tried to
79 investigate the stress state and failure process of loaded rock through infrared
80 radiation temperature fields, infrared radiation mechanisms of rock were

simultaneously revealed. Initially, the evolution of infrared thermograms of rocks in the failure process was observed by some researchers. For example, Wu et al. (2006a) conducted a series of tests on rock under uniaxial stress, compressive shear, biaxial stress, frictional slide and impact. It is found that highlighted infrared radiation temperature (IRT) is prone to appear at fracturing center of compressively loaded rock and shear zone. Therefore, the thermoelastic effect and the frictional-thermal effect are main mechanisms that cause the infrared radiation image abnormalities. Subsequently, on the basis of the infrared thermograms, IRT fields were quantitatively investigated. Wu et al. (2006b) further studied IRT fields of rock under uniaxial and biaxial load and compressive shear. Several IRT abnormalities were summarized on the basis of the average infrared radiation temperature (AIRT) curves, which can be seen as precursors for rock fracturing and failure. Li et al. (2018) researched the precursor information of coal and rock failure through the maximum IRT and AIRT curves. After the main rupture of the sample, it was found that the maximum ITR increased dramatically, while AIRT curves show obvious hysteresis in reaching the first peak value after the main rapture. For jointed rock with different fissure angles, Cheng et al. (2018) found that the effect of fissure angle on the maximum IRT and AIRT is similar with that on the normal load. The changes of the maximum IRT and AIRT simultaneously reach the peak value when fissure angle is 60 deg. Furthermore, the relationship between stress state of rock and IRT during the loading was explored. Nevertheless, previous studies normally focused on the whole IRT fields of rock

under the loading, the aforementioned quantitative indices reflect the overall change of rock surface. Thermal characteristics of rock at the local area such as the crack tips and trajectories of cracks in the fracture process are still unclear.

In the present study, a series of indention test were conducted on jointed rock specimens to investigate the thermal effects of jointed layer under concentrated load. During the test, strain and IRT fields of specimens were recorded by digital image correlation (DIC) system and infrared camera, respectively. Subsequently, comparison between strain and IRT fields were undertaken. Unlike the previous investigation, a new understanding on the IRT mechanism of jointed rock is presented. In addition, new thermal criteria for crack propagation were proposed for different crack types based on the maximum temperature gradient and the minimum temperature gradient. Besides revealing crack initiation, propagation and coalescence processes, and temperature concentration effects of jointed rock layer.

2 Experimental Methodology

2.1 Preparation for Specimen and Rock Properties

Granite block collected from Hunan province, China was employed in the present experiment in view of its high sensitivity to temperature under mechanical loading. The granite was cut into 3 blocks with the dimension of 200 mm×140 mm×30 mm, as shown in Figure 1. According to the research conducted by Johnson (1985), the ratio of the specimen width to plastic zone depth should be larger than 6 in order to

122 eliminate the size effect in indentation experiments. Besides, Alehoseein et al. (2000)
123 have pointed out that the plastic zone depths of the granite is 2 mm. The minimum
124 ratio of the width to plastic zone depth is 15, which is much more than 6. Karekal
125 (2000) further pointed out that the depth of plastic zone is function of rock brittleness
126 and he proposed new equations considering strain softening behavior of rocks.
127 Therefore, the dimensions of specimens are reasonable. To fabricate the jointed rock
128 mass similar to that in the nature, rock mass samples were made on the basis of
129 method proposed by Yang et al. (2018a, b) and Zhao et al. (2019). In detail, 4 through
130 going cuts were made in granite block with the aid of water jet. The inclination and
131 spacing of flaws are 30 deg (from horizontal plane) and 50 mm, respectively. Then,
132 the cuts were filled with cement mortar, which is made of 32.5R cement, sand, water
133 and water reducer. Through several tests, it was found that the properties of cement
134 mortar with mass ratio of 1: 1.5: 0.4: 0.15 were well accorded with that of joint plane
135 in nature. Subsequently, specimens were maintained in the standard circumstance for
136 28 days to achieve the expected bonding strength. After that, the specimens were
137 grinded and polished. For the purpose of avoiding the influence of pore water on
138 temperature response under the loading, all specimens were dried in an oven at 50°C
139 for 24 hours, then they were placed in a desiccator for cooling. During the experiment,
140 deformation on the surface of jointed rock mass is measured by DIC system. As the
141 displacement of rock surface is calculated by tracing random speckles on the
142 specimens in DIC technique (Sutton et al. 2009; Munoz et al. 2016a), white paint was

143 firstly painted on the front surface of specimens to make a basecoat. Then, black paint
144 was sprayed randomly. After several treatments mentioned above, jointed rock
145 specimens were evenly fabricated. Properties of granite and jointed plane are listed in
146 Table 1.

147 2.2 Test Apparatus

148 Test apparatus employed in the present study consists of loading system, control
149 system, XTDIC-2D system, D384M infrared camera and isolating box, as shown in
150 Figure 2.

151 In detail, loading system is comprised of a MTS servo-hydraulic machine and a pair
152 of locally designed indenters. The loading capacity of both vertical and horizontal
153 cylinders installed in MTS servo-hydraulic machine is 600 kN and theirs full cylinder
154 stroke is 100 mm. A pair of indenters with spacing of 60 mm and tip width of 12 mm
155 is installed on the vertical platens to generate concentrated load on the fabricated rock
156 mass specimen. Indenters are made of H13 steel with hardness of 55 HRC. The
157 deformation of indenters under loading can be ignored when compared to the
158 deformation of the fabricated rock mass. The loading rate of the actuators
159 (0.001-10mm/min or 0.1-100kN/min) is controlled by the MTS console.

160 The deformation of rock block during the loading is captured by XTDIC-2D which is
161 a non-contact deformation measurement system. The measurement system consists of
162 a Basler acA2440-75um charge coupled device (CCD) camera and a Light-Emitting

Diode (LED) light with luminous flux of 18000 lm. The CCD camera has a resolution of 2448 × 2048 pixels and a frame rate of 75 fps. As light spectrum of LED illuminant does not contain infrared, IRT of jointed rock mass specimens is not affected by LED light (Liu et al. 2018). The field of view and accuracy of XTDIC-2D system is 10 m×10 m and 0.01pixel, respectively.

D384M infrared camera is used to measure the IRT of the rock surface in the experiment. The specifications of D384M are as follows: resolution, 384 × 288 pixels; noise-equivalent temperature difference, 0.045 K, frame rate, 12 fps; temperature range, -20-150 degC, 100-650 degC; field of view, 28.4° ×21.5°; spectral range, 8-14 μm. In addition, to eliminate the influence of environmental interference, an isolating box with 1.5 m in length, 0.3 m in width and height is prepared (Sun et al. 2017). The isolating box is made of cystosepiment, which provide good heat insulation.

2.3 Experimental Process

In the present investigation, a series of indention tests were performed on the jointed rock mass specimens to simulate the cracking process of jointed rock layer under the concentrated load. Detailed experimental procedures are as follows:

(1) Specimens were firstly placed in laboratory for over 24 hours, thus the temperature of jointed rock specimens is equal to room temperature (Li et al. 2018, Ma & Sun, 2018). In order to reduce the end friction between the specimen and platens, the side and bottom of specimens were lubricated by silicon grease prior to

183 loading.

184 (2) The specimen is placed in the isolating box, CCD camera and D384M infrared
185 camera lie 0.8 m away from the front and back of specimens, respectively.

186 (3) Before loading, a horizontal uniform load of 8.4 kN was applied on the side
187 surfaces of specimen, which represents the confining stress of 2MPa in underground.
188 Then the specimen is preloaded with vertical load of 1 kN for 10 min until no further
189 surface deformation is observed in the granite block. Infrared camera was kept in 'on'
190 mode well in advance in order to monitor the IRT field of specimen until it stabilizes.

191 (4) The vertical cylinder in MTS servo-hydraulic universal machine, CCD camera and
192 infrared camera were manually triggered simultaneously. Time intervals of triggering
193 these systems keep within 0.5 s. In the indention process, the vertical cylinder is
194 controlled in displacement manner with loading rate of 0.5 mm/min. Normal force
195 and penetration depth were measured by sensors in MTS servo-hydraulic machine in
196 real time. Horizontal confining stress was kept constant at a value of 2MPa. The
197 frame rate of CCD camera is set to 1 Hz. Infrared radiation video was recorded by
198 infrared camera in time.

199 (5) The experiment was terminated when penetration depth reached 10 mm.

200 In addition, to further reduce the environment interference, personnel walking around
201 experimental rig was forbidden in the laboratory.

2.4 Data Analysis

In the experiment, normal force applied on indenters, penetration depth, photographs captured by CCD camera and infrared radiation video were recorded. Due to the discreteness of experimental results, the most representative data among the three tests were segregated.

Data analysis involved calculation and analysis of both the strain fields and the differential infrared thermograms of jointed granite block. In consideration of the advantages of reducing environmental interference and uneven emissivity of the rock sample surface, the differential thermograms were calculated to analyze the thermal characteristics of rock samples. The method for calculating differential thermograms is illustrated in Figure 3. The infrared thermograms at any time can be obtained using D384M software. The thermogram is comprised of an IRT matrix of size of 288 × 384, and is expressed as $\mathrm{IRT}^{(1)}_{384\times288}$. Then the valid matrix $\mathrm{IRT}^{(1)}_{m\times n}$ was selected from $\mathrm{IRT}^{(1)}_{384\times288}$ using MATLAB code to correspond to IRT of the rock surface at particular location and time. Similarly, a valid matrix at initial time can be obtained, which is expressed as $\mathrm{IRT}^{(0)}_{m\times n}$. By subtracting $\mathrm{IRT}^{(1)}_{m\times n}$ and $\mathrm{IRT}^{(0)}_{m\times n}$, differential matrix $\Delta\mathrm{IRT}^{(1)}_{m\times n}$ is calculated. Eventually, with the aid of MATLAB, the differential thermogram corresponding to $\Delta\mathrm{IRT}^{(1)}_{m\times n}$ is extracted. It should be noted that differential thermograms had to be further rotated by 180 deg around its vertical central axis in order to match with the images captured by CCD camera.

3 Results

In this section, the fracture process of jointed rock layer under concentrated load was shown at first. Given that the focus of present study is on the temperature response of different types of cracks, only the infrared radiation characteristics of cracks in the initiation and propagation processes were analyzed along with the strain fields.

3.1 Cracking Behavior of Jointed Rock under Concentrated Load

In order to investigate the cracking behavior under concentrated load, crack initiation, propagation and coalescence processes of cracks beneath the left indenter are examined using the strain fields computed from the CCD camera images. Subsequently, on the basis of strain contours, crack types are determined.

Fracture processes of cracks beneath the left indenter are depicted in Figure 4. Figure 4a shows the initial state of rock specimen in the test. With increase in the concentrated load, the normal and shear stresses also increase, resulting in shear deformation of the joint plane. The joint shear deformation produced a small tensile kink perpendicular to the joint plane in the region beneath the left indenter at 120 s, as illustrated in Figure 4b. Further loading, the kink propagated obliquely producing a main crack which eventually propagated towards the indenter tip at 122 s (Figure 4c). At the same time, indenter penetration resulted in the formation of tensile stresses at the free surface at a distance from an indenter. When these tensile stresses equated to the tensile strength of granite, a secondary crack (conical crack) is emanated from the

242 rock free surface and propagated towards the nearest joint plane. Two seconds later
243 (i.e. 124 s), secondary crack reached joint plane (Figure 4d).
244 Strain contours corresponding to Figure 4a, b and c are calculated by DIC technique,
245 as depicted in Figure 5. Contours of horizontal strain, vertical strain and shear strain
246 are included. The positive values of horizontal and vertical strains represent the
247 tensile strain while the negative values denote compressive strain. For horizontal
248 strain contours (Figure 5a), obvious tensile strain concentration zone could be
249 observed between the left indenter and joint plane when the main crack is initiated
250 (120 s). After that, tensile strain concentration area continued to propagate. At the
251 secondary crack region, horizontal strain along the crack trajectory is little larger than
252 other zone. However, in vertical strain field shown in Figure 5b, no obvious strain
253 concentration is observed at both the trajectories of main and secondary cracks. In
254 shear strain field (Figure 5c), zone of shear strain concentration only appears at the
255 location of main crack. While along the secondary crack, variation of shear strain is
256 not obvious in the cracking process. From the strain fields, it is concluded that the
257 main crack occurs due to the tensile and shear stress, while the secondary crack is
258 mainly caused by tensile stress. Therefore, patterns of main and secondary cracks are
259 the mixed shear-tensile and the tensile cracks, respectively.
260 To better illustrate the thermal effect of fracture process for different types of cracks,
261 main and secondary cracks depicted in Figure 4 will be respectively renamed as the
262 mixed shear-tensile and the tensile cracks in the sections below.

3.2 Thermal Features during the Initiation of Mixed Shear-tensile Crack and Tensile Crack

In geological engineering, to detect the position of crack initiation and avoid the disaster, it is necessary to understand the thermal features of crack initiation processes with different crack types. Consequently, on the basis of the evolutions of infrared thermograms and IRT at initiation points of crack, the thermal features of crack initiation are shown in this section.

During the experiment, the infrared thermograms of rock sample surface were recorded in the fracture process. Differential thermograms at time of crack initiation (120 s and 122 s) are depicted in Figure. 6. Besides, to highlight the temperature variations in local area, a term "temperature concentration factor (TCF)" is introduced, which is given by

$$\mathrm{TCF}_t = \frac{\Delta \mathrm{IRT}_{i,j,t}}{\Delta \mathrm{AIRT}_t} \tag{1}$$

where $\Delta \mathrm{IRT}_{i,j,t}$ denotes the differential infrared radiation temperature of a point (i, j) at the time t, $\Delta \mathrm{AIRT}_t$ represents the differential average infrared radiation temperature of the whole rock surface at the time t. $\Delta \mathrm{IRT}_{i,j,t}$ and $\Delta \mathrm{AIRT}_t$ can be obtained from differential thermograms. Larger TCF value indicates higher temperature at the studied point compared with the average temperature on the whole rock surface.

Figure 6 also depicts TCF at initiation points of the mixed shear-tensile crack (point

A) and tensile crack (point B) as a function of time. For the mixed shear-tensile crack, it is found that TCF increase gradually before 120 s. Then the value rises dramatically from 1.29 to 1.71. Accordingly, highlighted temperature localization zone appears at point A when t=120 s. However, the variation of TCF at initiation point of the tensile crack shows a different trend. From 0 to 122 s, TCF generally decrease from 1.50 to 1.14, but at the time of crack initiation (122 s), TCF reaches the minimum value of 1.00. At this time, no obvious temperature localization zone appears at the initiation point for the tensile crack. In contrast, along the mixed shear-tensile crack, high temperature zone extends to the free surface near the indenter region.

That is to say, the sudden appearance of high temperature zone extends could be seen as the temperature characteristic of the mixed shear-tensile crack initiation. For the tensile crack, however, the highlighted temperature zone is not obvious because the temperature reaches the minimum value at the time of rupture.

4 Discussion

The thermomechanical coupling effect is defined as the heat production in a solid due to stress action. Therefore, thermal features of jointed rock layer under concentrated load are closely related to the stress conditions. In this part, with the aim to reveal the correlation between stress and IRT at jointed rock layer during the crack initiation, and propagation processes, comparison between strain fields and differential thermograms in the cracking process are made. Then, based on the thermomechanical

303 coupling effect, the mechanism of IRT characteristics at crack initiation points is
304 explained. In addition, new criteria for the crack propagation from thermal
305 perspective are proposed. Finally, thermal concentration effect at both crack initiation
306 and coalescence points are described.

307 ### 4.1 Comparison Between Strain fields and Differential Thermograms during
308 Cracking Processes

309 During the infrared detection process, it is necessary to identify the hidden features in
310 layer on the basis of infrared fields. To investigate the relation between thermal
311 features of jointed layer at their failure region and corresponding cracking behaviors,
312 comparisons between differential thermograms and strain fields are made.
313 The evolutions of infrared radiation fields and corresponding strain fields in cracking
314 process are illustrated in Figures 6 and 5 respectively. For the mixed shear-tensile
315 crack, it is found that highlighted temperature localization zone extends from point A
316 to the zone beneath the left indenter in the crack initiation and propagation processes.
317 Correspondingly, tensile and shear strain concentrations appear along the trajectory of
318 the crack. However, for the tensile crack, no obvious high temperature zone appears
319 along the crack. From strain fields, it can be seen that tensile strain accumulation in
320 the tensile crack region is much larger than the shear strain.
321 By comparison, it is concluded that the shear deformation of crack plays a decisive
322 role in the highlighted temperature localization. This can be explained by the

323 frictional-thermal effect, which means the heat production caused by friction between
324 rock grains and micro friction of closed micro-cracks inside the rock. To investigate
325 the shear deformation mode of cracks, 5 evenly distributed points each along the
326 mixed shear-tensile crack and side tensile crack are selected, as shown in Figure 7.
327 These points are numbered from 1 to 10 in sequence. The variations of shear strain for
328 the mixed shear-tensile and tensile cracks are illustrated in Figure 8 (a) and (b),
329 respectively. By comparison, it is seen that shear strain along the mixed shear-tensile
330 crack increase gradually after 100 s, indicating friction between rock grains and
331 between microcracks. After 120 s, shear strain increases dramatically followed by
332 macro-crack formation. More friction heat is produced, causing obvious temperature
333 concentration zone along the crack trajectory, whereas the shear strain in the tensile
334 crack region maintains stable during the whole experiment, therefore, the
335 frictional-thermal effect is not seen in the cracking process. This has some
336 implications in the geological prospecting. The shear deformation of strata is
337 commonly encountered (e.g., landslide, slope stability, fault movement in earthquakes
338 or reservoir induced seismicity). Locations of shear failure in strata can be found
339 according to the highlighted temperature localization zone in IRT fields.

340 ### 4.2 Understanding of IRT Mechanism of Jointed Rock Layer Induced by
341 Stress at Crack Initiation Points

342 Wu et al. (2006a) pointed out that the thermoelastic effect and the frictional-thermal

343 effect are two of the main mechanisms that affecting the IRT of loaded rock. Although
344 the IRT mechanism of rock has been investigated by many researches, thermal
345 features at crack initiation points are not captured properly. Therefore, in this study,
346 stress states of crack initiation points are firstly determined on the basis of strain fields.
347 Then, according to the thermoelastic effect and the frictional-thermal effect, the
348 influence of stress on IRT mechanism at the point of crack initiation in jointed rock
349 layers is explored.

350 Overall, the thermomechanical coupling effect is divided into thermoelastic,
351 thermoplastic and thermoviscous effects (Harwood and Cummings, 1991). Due to the
352 obvious brittleness and high compression strength of tested granite sample, the plastic
353 and viscous deformation of rock could be ignored (Wu et al. 2006a). In addition,
354 study conducted by Chen et al. (2015) shows that pure shear deformation is a plastic
355 deformation, which could not produce any heat in the early stages of loading.
356 Therefore, only the thermoelastic effect is taken into consideration before the crack
357 initiation process. According to the thermoelastic effect, relationship between surface
358 physical temperature change and the stress is:

359 $$\Delta T = -\frac{\alpha}{\rho C_p} T \Delta\left(\sigma_1 + \sigma_2 + \sigma_3\right) \tag{2}$$

360 where ΔT is the change of temperature in K, T refers to absolute temperature of the
361 surface of the solid, in K, α represents the factor of linear thermal expansion in K^{-1}, ρ
362 stands for density of solid (Kg/m^3), C_p denotes the heat capacity of solid at normal

363 atmosphere ($J \cdot kg^{-1}\ K^{-1}$), $\Delta(\sigma_1+\sigma_2+\sigma_3)$ is the sum of principal stress in MPa. It
364 should be noted that $\sigma<0$ represents compressive stress. That is to say, the
365 temperature of the solid will be increased under the compression and it would be
366 reduced under the tension. Beside, in this experiment, jointed rock mass sample is
367 loaded under plane stress, thus σ_2=0.

368 In the plane stress problem, σ_1 and σ_3 are expressed as:

369
$$\left.\begin{matrix}\sigma_1\\ \sigma_3\end{matrix}\right\}=\frac{\sigma_x+\sigma_y}{2}\pm\sqrt{\left(\frac{\sigma_x+\sigma_y}{2}\right)^2+\tau_{xy}^2} \tag{3}$$

370 Since principal stress coincide with x and y direction in the experimental set up, and
371 they can be related as:

372
$$\sigma_1+\sigma_3=\sigma_x+\sigma_y \tag{4}$$

373 By substituting Equation 4 into Equation 2, ΔT can be calculated

374
$$\Delta T=-\frac{\alpha}{\rho C_p}\Delta(\sigma_x+\sigma_y) \tag{5}$$

375 To explore the stress conditions of jointed rock, the horizontal, vertical and shear
376 strains (corresponding to ε_x, ε_y and γ) at initiation points for the mixed
377 shear-tensile crack and tensile crack are calculated through the DIC technology, the
378 results are present in Figure 9. In this figure, negative and positive ε_x or ε_y
379 represent compression and tensile deformation, respectively. From Figure 9, it is
380 concluded that the stress state at initiation point for the mixed shear-tensile crack
381 changes from biaxial compression to the horizontal tension-vertical compression in
382 the elastic stage. In the crack initiation process, frictional sliding of the crack takes

383 place. For the tensile crack, the stress state at initiation point changes from uniaxial
384 compression to uniaxial tension in the whole loading process, frictional sliding is not
385 obvious during the crack initiation.

386 According to stress states mentioned above, in the case of the mixed shear-tensile
387 crack, the thermoelastic effect is the main factor influencing the IRT of initiation point
388 just before the failure occurs. During the crack initiation process, the
389 frictional-thermal effect is more prominent. As for the tensile crack, the IRT is only
390 determined by the thermoelastic effect.

391 In elastic stress state, ε_x and ε_y are calculated using generalized Hooke's Law as
392 follows:

393
$$\begin{cases} \varepsilon_x = \dfrac{1}{E}(\sigma_x - \mu\sigma_y) \\ \varepsilon_y = \dfrac{1}{E}(\sigma_y - \mu\sigma_x) \end{cases} \tag{6}$$

394 where E and μ are the Young's modulus and Poisson's ratio of rock, respectively. σ_x
395 and σ_y are horizontal and vertical stresses acting on the rock. Therefore, σ_x and
396 σ_y is expressed as:

397
$$\begin{cases} \sigma_x = \dfrac{1}{1-\mu^2}(E\varepsilon_x + \mu E\varepsilon_y) \\ \sigma_y = \dfrac{1}{1-\mu^2}(E\varepsilon_y + \mu E\varepsilon_x) \end{cases} \tag{7}$$

398 According to ε_x and ε_y obtained from DIC technology, σ_x and σ_y can be
399 calculated using Equation (7). For the mixed shear-tensile crack, ε_y is much larger
400 than ε_x in the elastic stage. In addition, from equation (5), it is deduced that:

401 $$\Delta T = \Delta T_x + \Delta T_y = -\frac{\alpha}{\rho C_p}\Delta\sigma_x - \frac{\alpha}{\rho C_p}\Delta\sigma_y \quad (8)$$

402 $$\frac{\Delta T_x}{\Delta T_y} = \frac{\Delta\sigma_x}{\Delta\sigma_y} \quad (9)$$

403 σ_x and σ_y obtained from DIC technology (Eq. 7) are equal to $\Delta\sigma_x$ and $\Delta\sigma_y$,
404 respectively. By substituting equation (7) into equation (9), the proportions of
405 temperature caused by horizontal and vertical stresses are obtained. The temperature
406 proportion for the mixed shear-tensile crack is shown in Figure 10. From this figure, it
407 can be observed that the proportion of ΔT_y continues to increase with time. But at
408 the time before crack initiation, horizontal strain becomes positive, causing the
409 reduction in temperature. Thus the proportion of ΔT_x is defined as positive. Whereas,
410 the proportion of ΔT_y at that corresponding time becomes numerically larger than
411 100%. That is to say, σ_y play a decisive role in heat production for the mixed
412 shear-tensile crack before the crack initiation. Vertical stress acting on the initiation
413 point of this crack increases continually (Figure 9b), causing the increase in the
414 temperature. As a result, TCF of the mixed shear-tensile crack increases gradually
415 before the failure. At the time just before the crack initiation, dramatic increase in γ
416 indicates the obvious frictional-thermal effect, leading to the sudden increase in TCF
417 and highlighted temperature zone on the rock surface. As for the tensile crack is
418 concerned, the IRT is only determined by the thermoelastic effect. Generally, the
419 horizontal stress acting on the initiation point varies from compression to tension, the
420 change of sum of principal stress is positive, causing the continue decrease in TCF, as

421 shown in Figure 6.

422 From the characteristics of TCF, the failure zone of jointed rock with different crack
423 types can be detected once the cracks initiate, especially the mixed shear-tensile crack
424 and shear crack. This phenomenon is found similar to that of results of Liu et al.
425 (2006), in which a uniaxial compression test and the compressively induced shearing
426 test were conducted on rock samples. At failure moment, it was found that both the
427 shear fractures were accompanied by highlighted IRT concentration. The main
428 reasons are attributed to the frictional-thermal effect.

429 ### 4.3 Crack Propagation Criteria based on Thermal Effects

430 In fracture mechanics, several criterions for crack propagation have been proposed
431 from the perspective of stress and energy, such as the maximum circumferential stress
432 criterion, the energy release rate criterion and the strain energy density criterion.
433 However, from thermal point of view, the crack propagation criteria have been
434 scarcely studied. In this section, the maximum temperature gradient criterion and the
435 minimum temperature gradient criterion are firstly proposed according to IRT results.
436 Based on these criteria, the direction of crack propagation can be determined.

437 To compare IRT at zones nearby the crack tips with that at point 1-10, 8 circles or
438 semicircles which numbered I, II, III, IV, VI, VII, VIII and IX were selected, the
439 corresponding centers of them are point 1, 2, 3, 4, 6, 7, 8 and 9, respectively (Figure
440 7). Radii of circles or semicircles are equal to the distance between the adjacent points

441 on crack trajectories. Therefore, variations of differential temperature $\Delta\mathrm{IRT}$ at these
442 points with time, before crack coalescence, were calculated. After that, the term
443 "temperature gradient" is proposed. It reflects the change in temperature over the
444 circle or semicircle, which is obtained by

445 $$G_{Ti} = \frac{\Delta\mathrm{IRT}_{i+1} - \Delta\mathrm{IRT}_i}{r_i} \quad (i=1,\ 2,\ 3,\ 4,\ 6,\ 7,\ 8,\ 9) \tag{10}$$

446 Where G_{Ti} is the temperature gradient at zones around point i, $\Delta\mathrm{IRT}_i$ and $\Delta\mathrm{IRT}_{i+1}$
447 represent the differential temperature at i th point and (i+1) th point on circle or
448 semicircle, respectively. r_i is radius of i th circle or semicircle.

449 From Equation 10, the temperature gradient at any time is calculated. Subsequently,
450 average temperature gradients from 0 s to the time just before crack coalescence are
451 obtained, as illustrated in Figure 11. Obviously, for each circle or semicircle along the
452 shear-tensile crack, the average temperature gradient at the time of failure is larger
453 than others points. On the contrary, in the case of the tensile crack, the average
454 temperature gradient at the time of failure is the minimum. In another word, the mixed
455 shear-tensile crack propagates toward the direction where the average temperature
456 gradient is maximum, while the tensile crack propagates toward the direction where
457 the average temperature gradient is minimum, and these are termed as "the maximum
458 temperature gradient criterion" and "the minimum temperature gradient criterion",
459 respectively.

460 The criteria can be explained by the thermoelastic effect and the frictional-thermal

461 effect. As mentioned in section 4.2, before the crack initiation, the thermoelastic effect
462 is considered as the main mechanism of heat production. From Equation 5, it can be
463 deduced that the change in IRT is a linear function of $\sigma_x+\sigma_y$. Similarly, "stress
464 gradient" around the crack tip is defined as below:

465 $$G_{Si} = \frac{\left(\sigma_x + \sigma_y\right)_{i+1} - \left(\sigma_x + \sigma_y\right)_i}{r_i} \quad (i=1, 2, 3, 4, 6, 7, 8, 9) \tag{11}$$

466 Where G_{Si} represents the stress gradient at zones around point i, $\left(\sigma_x + \sigma_y\right)_i$ and
467 $\left(\sigma_x + \sigma_y\right)_{i+1}$ are the sum of horizontal and vertical stress at ith point and (i+1)th point
468 (i.e., circle or semicircle), respectively. Similarly, average stress gradients from 0 s to
469 the time just before crack coalescence are calculated, as shown in Figure 11. For
470 points at the same circles or semicircles, strong correlation between temperature
471 gradient and stress gradient along the cracks can be found. Especially, the average
472 stress gradients at the mixed shear-tensile is smaller than that of at other points, while
473 the values at tensile cracks are larger than other points. This phenomenon indicates
474 that the compressive stress dominates the trajectory of the mixed shear-tensile crack,
475 negative stress gradient stands for the increase in compression. As a result,
476 temperature along the shear-tensile crack is larger than other zone. In the crack
477 propagation process, frictional-thermal effect also leads to the increase in temperature.
478 Subsequently, heating zone occurs along the shear-tensile crack. However, for the
479 tensile crack, positive stress gradient represents the increase in tensile, causing
480 reduction in temperature in that zone. Temperature fields along the cracks are

481 illustrated in Figure 12. Consequently, compared with IRT with other zone, the
482 temperature gradients along the mixed shear-tensile crack is the maximum, while the
483 value along the tensile crack trajectory is the minimum.

484 4.4 Temperature Concentration Effects during the Different Cracking Stages

485 In the present study, a new phenomenon is observed that the cracks show various
486 temperature concentration characteristics during the crack initiation, propagation and
487 coalescence processes. To investigate the thermal features in cracking processes,
488 temperature concentration factors (TCFs) of each point along the cracks (points 1-10
489 in Figure 7) are calculated. Regrettably, the trends of TCFs for each point cannot be
490 distinguished directly. Therefore, variances of TCFs from 0 s to the rupture time are
491 further calculated, results are shown in Figure 13a.

492 In Figure 13a, it is found that the variance trends of TCFs for the mixed shear-tensile
493 and tensile cracks are similar with each other. For each crack, variances of TCFs at
494 crack initiation point (i.e. point 1 or 6) and crack coalescence point (i.e. point 5 or 10)
495 are obviously more than that at other points. The phenomenon indicates that the
496 temperature change during crack initiation and coalescence processes is more
497 pronounced than that in crack propagation process.

498 To explain the temperature concentration effects during the different cracking stages,
499 the variances of $\Delta\left(\sigma_x+\sigma_y\right)$ for the corresponding points are calculated, and the
500 results are illustrated in Figure 13b. By comparison, it is seen that the variances of

TCF and $\Delta\left(\sigma_x+\sigma_y\right)$ have similar trends. Study done by Ma et al. (2018) also found that the sudden changes in successive minus infrared image temperature often accompanied with sudden changes in stress. Before the crack initiation, no obvious flaws appear at the initiation points, so more stress is needed to achieve stress concentration at the initiation points as ΔIRT is proportional to $\Delta\left(\sigma_x+\sigma_y\right)$. In addition, from Figure 8, it is also found that obvious shear deformation takes place for the mixed shear-tensile crack at the time of crack initiation. As a result, dramatic change in IRT occurs during crack initiation stage. After that, cracks propagate stably, causing the reduction in the variation of $\Delta\left(\sigma_x+\sigma_y\right)$. At the time of crack coalescence, the mechanisms of stress change for the mixed shear-tensile and tensile cracks differ. Overall, for the mixed shear-tensile crack, when the crack passes through the rock, stress at crack tip disappears suddenly, causing the dramatic decrease in IRT. However, for the tensile crack, when crack coalesces with the jointed plane, concentrated stress at the crack tip overlay the stress along the jointed plane, leading to the sudden increase in stress at crack coalescence point. The dramatic change in IRT at crack initiation and coalescence points will be favorable for determining the failure zone in jointed rock layers.

5 Conclusions

In the present study performs a series of indention tests on the jointed rock specimens were performed to understand the fracture process of jointed layer under concentrated

load based on thermal characteristics and strain field characteristics. Thermal effects in crack initiation, propagation and coalescence processes were investigated. Based on the experimental results, some new understandings of infrared radiation features of cracking processes in jointed rock mass are concluded as follows:

1. Comparisons between the strain fields and differential thermograms in cracking processes indicate that the highlighted temperature localization in IRT fields mainly caused by the frictional-thermal effect, while the effects of tensile and compressive stresses are not quite conspicuous.

2. Based on the stress states obtained from DIC technique, ITR mechanisms at crack initiation crack were highlighted. For the mixed shear-tensile crack, thermoelastic effect and the frictional-thermal effect were dominant and they influence the IRT distribution at the time of crack initiation and propagation. Whereas in case of tensile crack, the IRT is only determined by the thermoelastic effect in cracking process.

3. The mixed shear-tensile crack and tensile crack propagate following the maximum temperature gradient criterion and the minimum temperature gradient criterion, respectively. The new thermal criteria are in congruent with that of the stress gradient along the crack trajectories.

4. High variations in the IRT at crack initiation points and coalescence points are observed than at other regions. Further, a strong correlation between the stress gradient and the temperature gradient during the crack initiation and coalescence process is observed.

Acknowledgements

The financial support from Project supported by graduate research and innovation foundation of Chongqing, China (Grant No.CYB19015), Natural Science Fund of China (Nos. 51879016) and the National Key R&D Program of China, No.2018YFC1505504) are greatly appreciated. Data supporting this research are available in: https://data.mendeley.com/datasets/wy92dfnyds/draft?a=b1f355c9-7765-462c-86f2-77b4ed47b574. The authors declare no conflict of interest. No financial and personal relationships with other people or organizations that can inappropriately influence our work.

References

Alehoseein, H., Detournay, E., & Huang, H. (2000), An analytical model for the indentation of rocks by blunt tools. *Rock Mechanics and Rock Engineering,* 33(4), 267-284. doi:10.1007/s006030070003

Bosea, N., & Mukherjee, S. (2020), Estimation of deformation temperatures, flow stresses and strain rates from an intra-continental shear zone: The Main Boundary Thrust, NW Himalaya (Uttarakhand, India). *Marine and Petroleum Geology*, 112, 104094. doi:10.1016/j.marpetgeo.2019.104094

Chen, S., Liu, P., Guo, Y., Liu, L., & Ma, J. (2015), An experiment on temperature variations in sandstone during biaxial loading. *Physics and Chemistry of the Earth*, 85-86, 3-8. doi:10.1016/j.pce.2014.10.006

562 Chen, S., Liu, P., Liu, L., & Ma, J. (2013), A phenomenon of ground temperature change prior to
563 Lushan earthquake observed in Kangding. *Seismolog and Geology*, 35(3), 634-640.
564 doi:10.3969/j.issn.0253-4967
565 Chen, S., Liu, P., Liu, L., & Ma, J. (2016), Bedrock temperature as a potential method for
566 monitoring change in crustal stress: Theory, in situ measurement, and a case history. *Journal*
567 *of Asian Earth Sciences*, 123, 22-33. doi:10.1016/j.jseaes.2016.03.018
568 Cheng, C., Li, Z., Li, G., Wei, Y., Yin, S., Liu, S., & Kong, Y. (2018), Influence of prefabricated
569 fissure angle on sandstone damage and infrared radiation temperature characteristics. *Journal*
570 *of Geophysics and Engineering*, 15(4), 1187-1196. doi:10.1088/1742-2140/aaacaf
571 Graham, C. M. & England, P. C. (1976), Thermal regimes and regional metamorphism in the
572 vicinity of overthrust faults: An example of shear heating and inverted metamorphic zonation
573 from southern California. *Earth and Planetary Science Letters*, 31(1), 142-152. doi:10.1016/
574 0012-821X(76)90105-9
575 Harwood, N., & Cummings, W. M. (1991), *Thermoelastic stress analysis.* Bristol: IOP Publishing
576 Ltd.
577 Johnson, K. L. (1985), *Contact mechanics.* Cambridge: Cambridge University Press.
578 Karekal, S. (2000), Analytical and experimental investigations of rock indentation process. In *9th*
579 *Annual JKMRC Conference*, pp. 107-138.
580 Li, H., Xue, L., Brodsky, E. E., Mori, J. J., Fulton, P. M., Wang, H., Kano, K., Yun, K., Harris, R.
581 N., Gong, Z., Li, C., Si, J., Sun, Z., Pei, J., Zheng, Y., & Xu, Z. (2015), Long-term
582 temperature records following the Mw 7.9 Wenchuan (China) earthquake are consistent with

583 low friction. *Geology*, 43(2), 163-166. doi:10.1130/g35515.1

584 Li, Z., Lou, Q., Wang, E., Liu, S., & Niu, Y. (2017), Study on acoustic-electric-heat effect of coal
585 and rock failure processes under uniaxial compression. *Journal of Geophysics and*
586 *Engineering*, 15(1), 71-80. doi:10.1088/1742-2140/aa8437

587 Li, Z., Yin, S. & Niu, Y. (2018), Experimental study on the infrared thermal imaging of a coal
588 fracture under the coupled effects of stress and gas. *Journal of natural gas science and*
589 *engineering*, 55, 444-451. doi:10.1016/j.jngse.2018.05.019

590 Liu, Q., Liu, Q., Pan, Y., Peng, X., Deng, P., & Huang, K. (2018), Experimental study on rock
591 indentation using infrared thermography and acoustic emission techniques. *Journal of*
592 *Geophysics and Engineering*, 15, 1864-1877. doi:10.1088/1742-2140/aac096

593 Liu, S., Wu, L., & Wu, Y. (2006). Infrared radiation of rock at failure. *International Journal of*
594 *Rock Mechanics & Mining Sciences*, 43, 972-979. https://doi.org/10.1016/j.ijrmms.2005.12.
595 009

596 Long, S., McQuarrie, N., Tobgay, T., & Hawthorne, J. (2011), Quantifying internal strain and
597 deformation temperature in the eastern Himalaya, Bhutan: implications for the evolution of
598 strain in thrust sheets. *Journal of Structural Geology*, 33, 579-608. doi:10.1016/j.jsg.2010.12.
599 011

600 Lu, X., Meng, Q., Gu, X., Zhang, X., Xie, T., & Geng, F. (2016), Thermal infrared anomalies
601 associated with multi-year earthquakes in the Tibet region based on China's FY-2E satellite
602 data. *Advances in Space Research*, 58(6), 989-1001. doi:10.1016/j.asr.2016.05.038

603 Ma, L., & Sun, H. (2018), Spatial-temporal infrared radiation precursors of coal failure under

604 uniaxial compressive loading. *Infrared Physics & Technology*, 93, 144-153. doi:10.1016/j.
605 infrared.2018.07.034
606 Ma, L., Sun, H., Zhang, Y., Hu, H., & Zgang, C. G. (2018), The role of stress in controlling
607 infrared radiation during coal and rock failures. *Strain*, 54, e12295. doi:10.1111/str.12295
608 Milne, J. (1886), *Earthquakes and Other Earth Movements.* New York: D. Appleton and Co.
609 Mukherjee, S. (2017), Shear heating by translational brittle reverse faulting along a single, sharp
610 and straight fault plane. *Journal of Earth System Science*, 126, 1-5. doi:10.1007/s12040-016-
611 0788-5
612 Mulchrone, K. F., & Mukherjee, S. (2016), Kinematics and shear heat pattern of ductile simple
613 shear zones with 'slip boundary condition'. *International Journal of Earth Sciences*, 105(3),
614 1015-1020. doi:10.1007/s00531-015-1206-y
615 Munoz, H., Taheri, A., & Chanda, E. K. (2016), Pre-peak and post-peak rock strain characteristics
616 during uniaxial compression by 3D digital image correlation. *Rock Mechanics and Rock*
617 *Engineering*, 49(7), 2541–2554. doi:10.1007/s00603-016-0935-y
618 Ramasamy, S. M., Gunasekaran, S., Rajagopal, N., Saravanavel, J. & Kumanan, C. J. (2019),
619 Flood 2018 and the status of reservoir-induced seismicity in Kerala, India. *Natural Hazards*,
620 99(1), 307-319. doi:10.1007/s11069-019-03741-x
621 Sanderson, D. J. (1982), Models of strain variation in nappes and thrust sheets: A review.
622 *Tectonophysics*, 88(3-4), 201-233. doi:10.1016/0040-1951(82)90237-2
623 Stiros, S. C. & Pytharouli, S. (2018), Interpretations of reservoir-induced seismicity may not
624 always be valid: The case of seismicity during the impoundment of the Kremasta Dam

(Greece, 1965-1966). *Bulletin of the Seismological Society of America*, 108(5B), 3005-3015. doi:10.1785/0120170359

Sun, H., Ma, L., Adeleke, N., & Zhang, Y. (2017), Background thermal noise correction methodology for average infrared radiation temperature of coal under uniaxial loading. *Infrared Physics and Technology*, 81, 157-165. doi:10.1016/j.infrared.2017.01.001

Sutton, M. A., Orteu, J. J., & Schreier, H. (2009), *Image correlation for shape, motion and deformation measurements*. Berlin: Springer.

Tramutoli, V., Aliano, C., Corrado, R., Filizzola, C., Genzano, N., Lisi, M., Martinelli, G. & Pergola, N. (2013), On the possible origin of thermal infrared radiation (TIR) anomalies in earthquake-prone areas observed using robust satellite techniques (RST). *Chemical Geology*, 339, 157-168. doi:10.1016/j.chemgeo.2012.10.042

Wu, L., Liu, S., Wu, Y. & Wang, C. (2006a), Precursors for rock fracturing and failure-Part I: IRR image abnormalities, *International Journal of Rock Mechanics & Mining Sciences*, 43, 473-482. doi:10.1016/j.ijrmms.2005.09.001

Wu, L., Liu, S., Wu, Y., & Wang, C. (2006b), Precursors for rock fracturing and failure-Part II: IRR T-Curve abnormalities. *International Journal of Rock Mechanics & Mining Sciences*, 43, 483-493. doi:10.1016/j.ijrmms.2005.09.001

Xiong, P., Shen, X., Gu, X., Meng, Q.,Bi, Y., Zhao, L., Zhao, Y., Li, Y., & Dong, J. (2015), Satellite detection of IR precursors using bi-angular advanced along-track scanning radiometer data: a case study of Yushu earthquake. *Earthquake Science*, 28(1), 25-36. doi:10.1007/s11589-015-0111-6

646 Yang, H., Li, Z., Jie, T., & Zhang, Z. (2018a), Effects of joints on the cutting behavior of disc
647 cutter running on the jointed rock mass. *Tunnelling and Underground Space Technology*, 81,
648 112-120. doi:10.1016/j.tust.2018.07.023
649 Yang, H., Liu, J., & Liu, B. (2018b), Investigation on the cracking character of jointed rock mass
650 beneath TBM disc cutter. *Rock Mechanics and Rock Engineering*, 51, 1263-1277.
651 doi:10.1007/s00603-017-1395-8
652 Zhao, Y., Yang, H., Chen, Z., Chen, X., Huang, L., & Liu, S. (2019), Effects of jointed rock mass
653 and mixed ground conditions on the cutting efficiency and cutter wear of tunnel boring
654 machine. *Rock Mechanics and Rock Engineering*, 52, 1303-1313.
655 doi:10.1007/s00603-018-1667-y

656 **Headings**

657 **1 Introduction**

658 **2 Experimental Methodology**

659 2.1 Preparation for Specimen and Rock Properties

660 2.2 Test Apparatus

661 2.3 Experimental Process

662 2.4 Data Analysis

663 **3 Results**

664 3.1 Cracking Behavior of Jointed Rock under Concentrated Load

665 3.2 Thermal Features during the Initiation of Mixed Shear-tensile Crack and Tensile

666 Crack

667 **4 Discussion**

668 4.1 Comparison Between Strain fields and Differential Thermograms during Cracking

669 Processes

670 4.2 Understanding of IRT Mechanism of Jointed Rock Layer Induced by Stress at

671 Crack Initiation Points

672 4.3 Crack Propagation Criteria based on Thermal Effects

673 4.4 Temperature Concentration Effects during the Different Cracking Stages

674 **5 Conclusions**

675

676 **Figure or Table Captions**

677 **Figure 1.** The picture of jointed rock mass sample (unit: mm).

678 **Figure 2.** Test system and experimental setup. (**a**) The positions of indenters and
679 jointed rock specimen, (**b**) experimental system, (**c**) the back of rock specimen, (**d**) the
680 front of rock specimen.

681 **Figure 3.** Schematic diagram of the methodology for calculating differential infrared
682 thermograms. Step 1: Extraction of IRT matrix of the whole image by IRT software.
683 Step 2: Extraction of IRT matrix at the rock mass zone. Step 3: Calculation of the
684 differential temperature. Step 4: Extracting the differential thermograms.

685 **Figure 4.** Cracking process of jointed rock under local stress at . (**a**) 0s; (**b**) 120 s; (**c**)
686 122 s; (**d**) 124 s.

687 **Figure 5.** The evolution of strain fields of jointed rock during the cracking. (**a**) The
688 horizontal strain. (**b**) Vertical strain. (**c**) Shear strain.

689 **Figure 6.** Curves of temperature concentration factors of initiation points for the
690 mixed shear-tensile and tensile cracks. The corresponding differential thermograms of
691 jointed rock mass at the time of crack initiation are depicted. Initiation points for the
692 mixed shear-tensile and tensile cracks are point A and point B, respectively.

693 **Figure 7.** The positions for data collection at the mixed shear-tensile crack and tensile
694 crack.

695 **Figure 8.** Variations of shear strain along (**a**) the mixed shear-tensile crack and (**b**)

tensile crack.

Figure 9. The variations of (**a**) horizontal strain, (**b**) vertical strain and (**c**) shear strain of mixed shear-tensile crack and tensile crack in cracking process.

Figure 10. The proportion of temperature caused by σ_x and σ_y at initiation points for the mixed shear-tensile crack.

Figure 11. Comparisons between average temperature gradients and stress gradients along the cracks, (**a**) the mixed shear-tensile crack, (**b**) tensile crack.

Figure 12. Temperature field along the cracks. Healing zone and cooling zone occur along the trajectories of the mixed shear-tensile crack and tensile crack, respectively.

Figure 13. Comparisons between (**a**) variances of temperature concentration factor and (**b**) $\left(\sigma_x + \sigma_y\right)$ for the mixed shear-tensile crack and tensile crack.

Table 1. Physical and mechanical properties of granite and jointed plane.

718

719

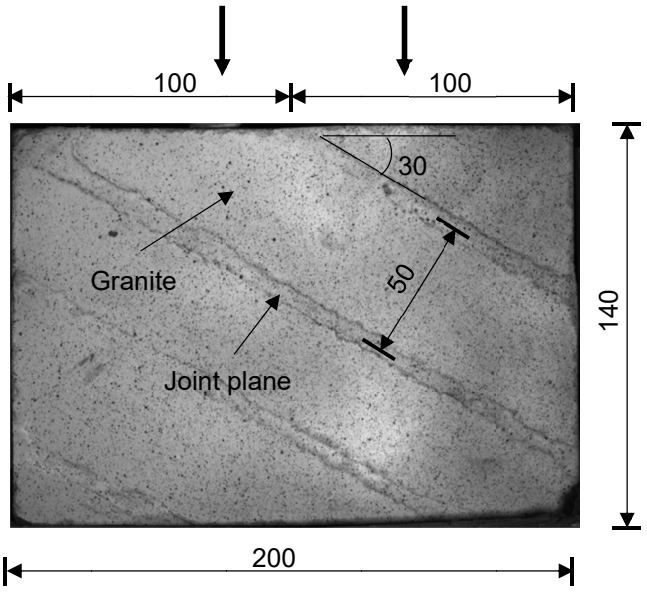

720

721 **Figure 1.** The picture of jointed rock mass sample (unit: mm).

722

Figure 2. Test system and experimental setup. (a) The positions of indenters and jointed rock specimen, (b) experimental system, (c) the back of rock specimen, (d) the front of rock specimen.

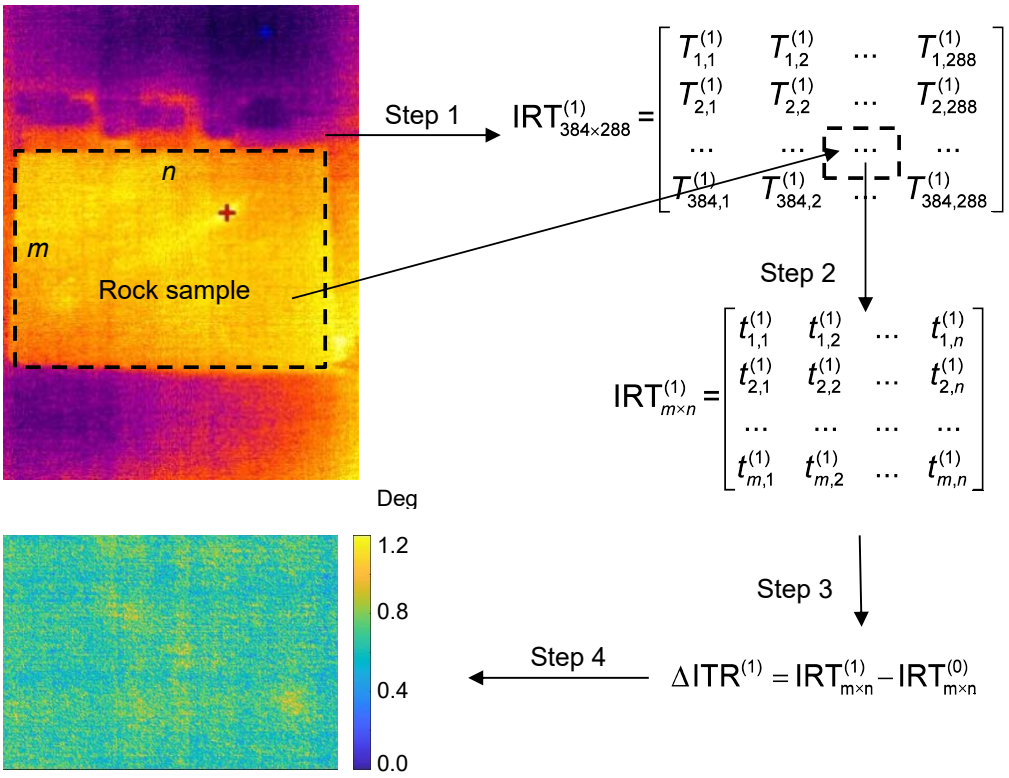

Figure 3. Schematic diagram of the methodology for calculating differential infrared thermograms. Step 1: Extraction of IRT matrix of the whole image by IRT software. Step 2: Extraction of IRT matrix at the rock mass zone. Step 3: Calculation of the differential temperature. Step 4: Extracting the differential thermograms.

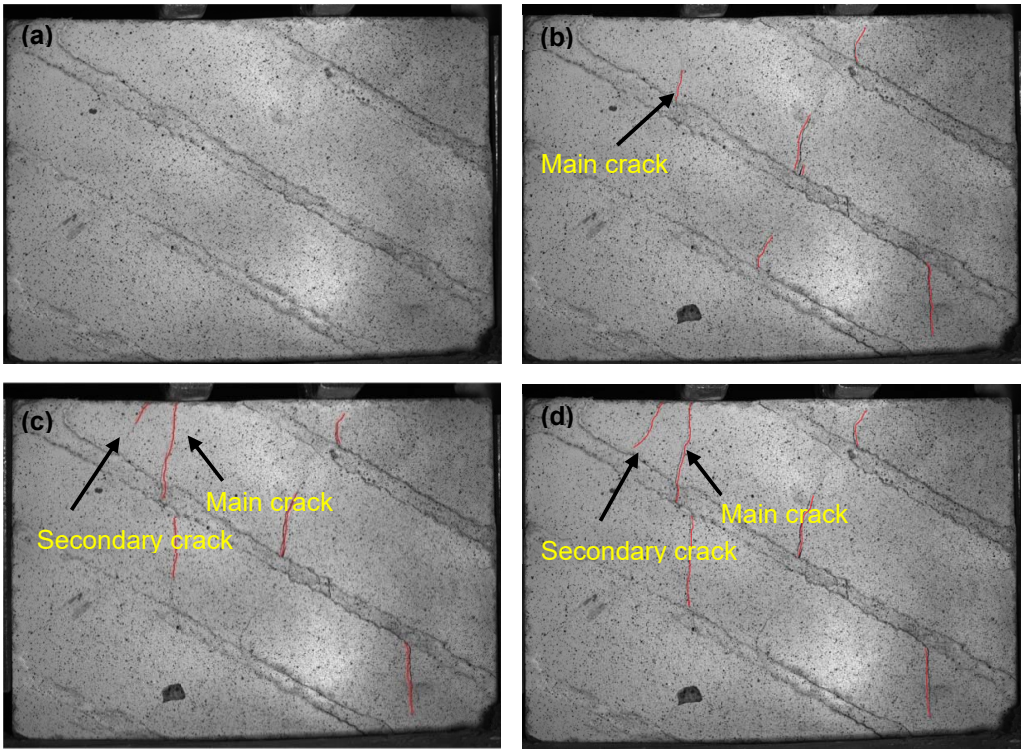

732

734 **Figure 4.** Cracking process of jointed rock under local stress at . (**a**) 0s; (**b**) 120 s; (**c**)

735 122 s; (**d**) 124 s.

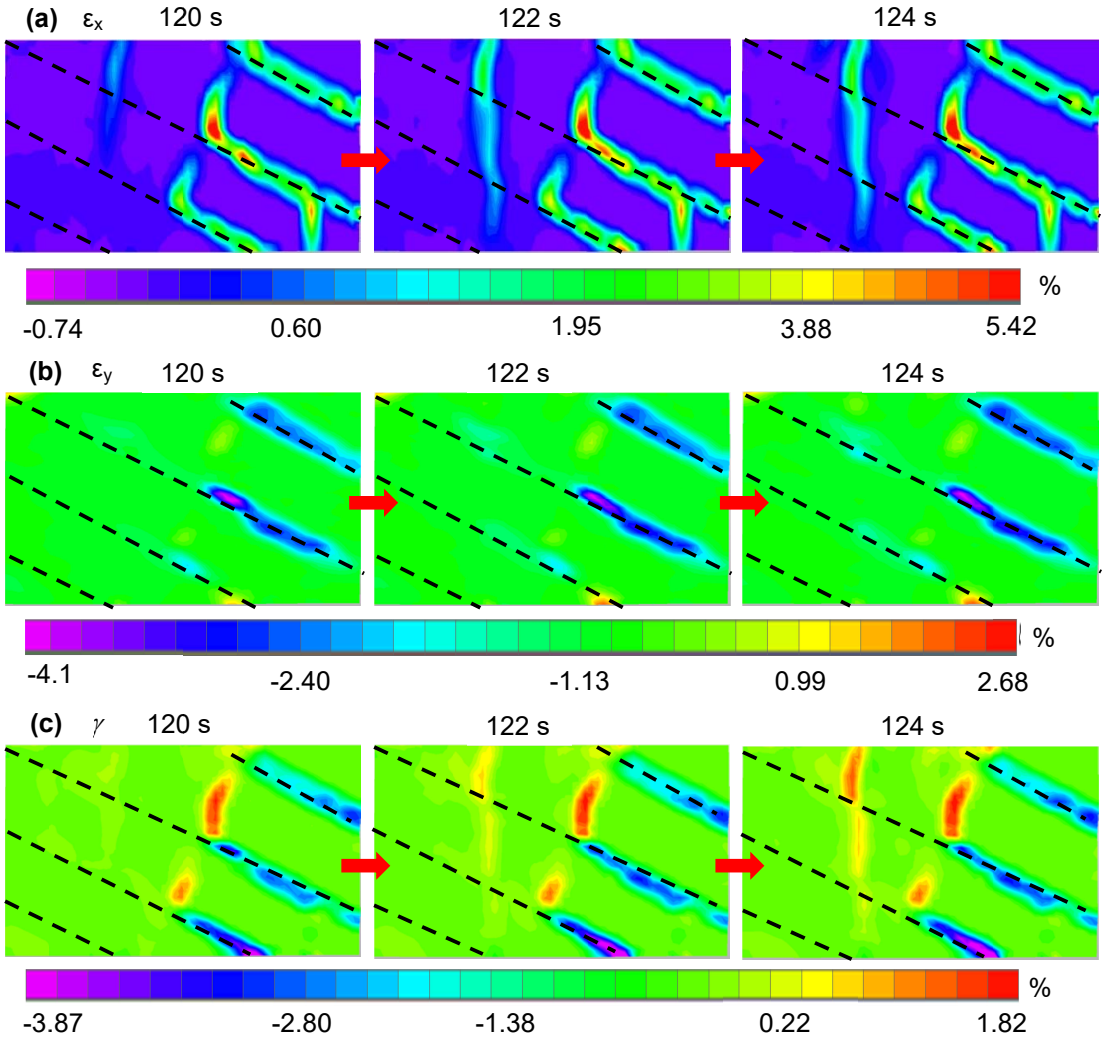

735

737 **Figure 5.** The evolution of strain fields of jointed rock during the cracking. (**a**) The

738 horizontal strain. (**b**) Vertical strain. (**c**) Shear strain.

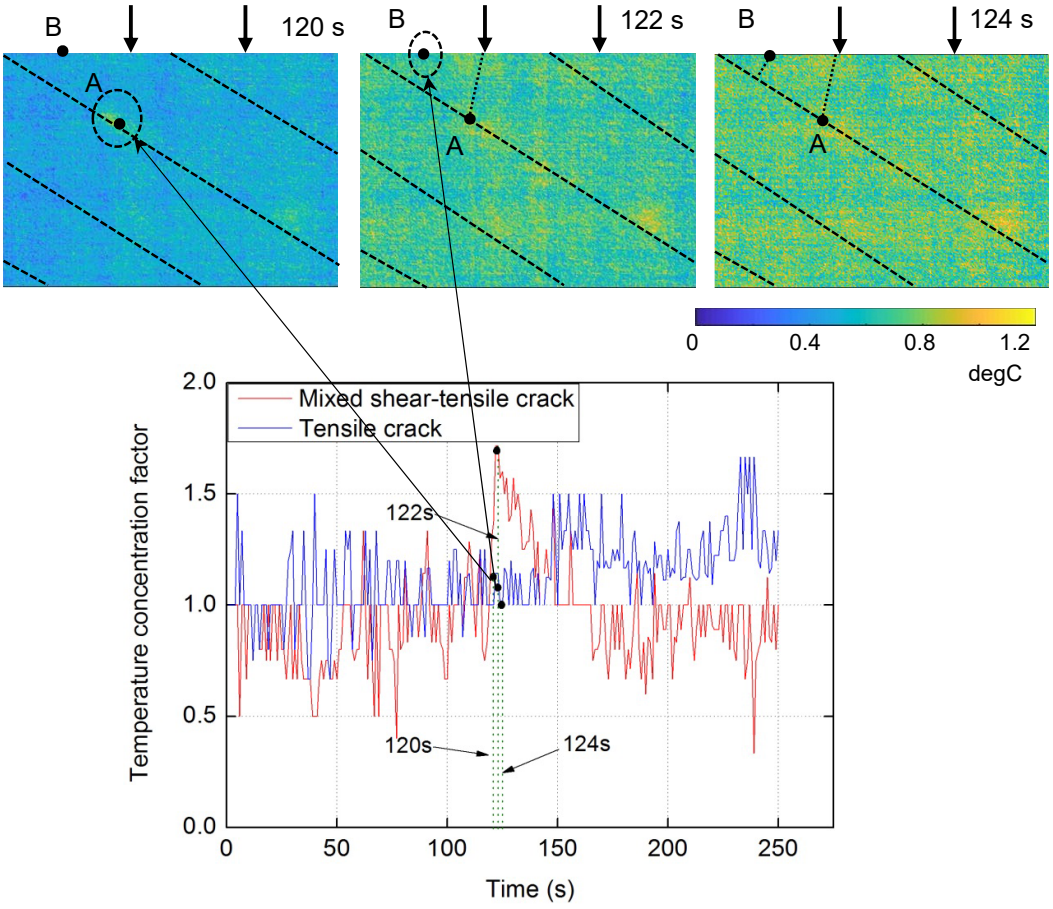

737

738 **Figure 6.** Curves of temperature concentration factors of initiation points for the
739 mixed shear-tensile and tensile cracks. The corresponding differential thermograms of
740 jointed rock mass at the time of crack initiation are depicted. Initiation points for the
741 mixed shear-tensile and tensile cracks are point A and point B, respectively.

742

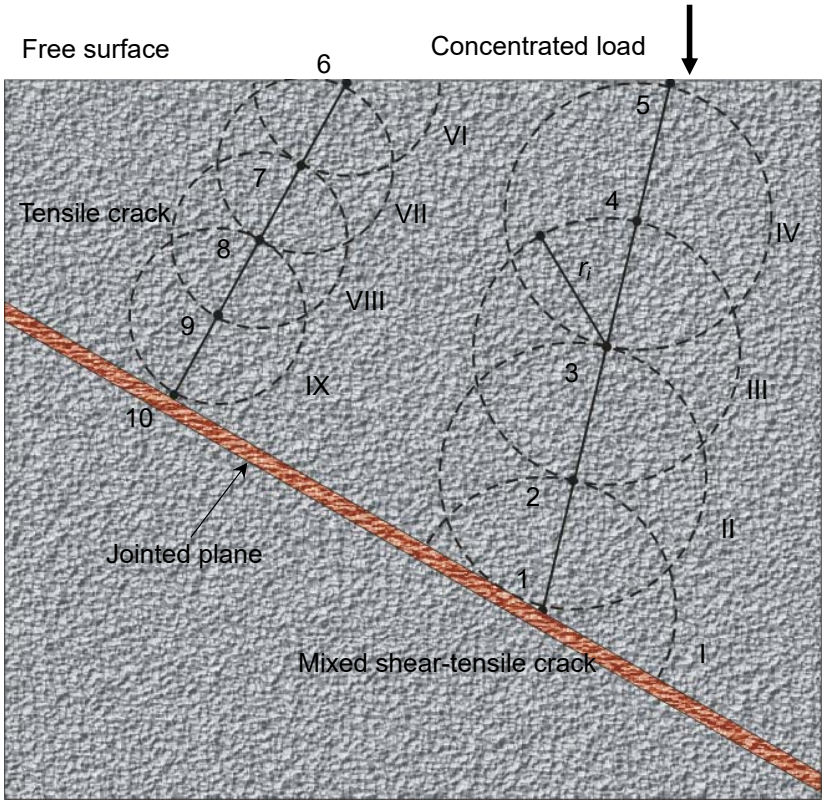

743

744 **Figure 7.** The positions for data collection at the mixed shear-tensile crack and tensile

745 crack.

746

747

748

749

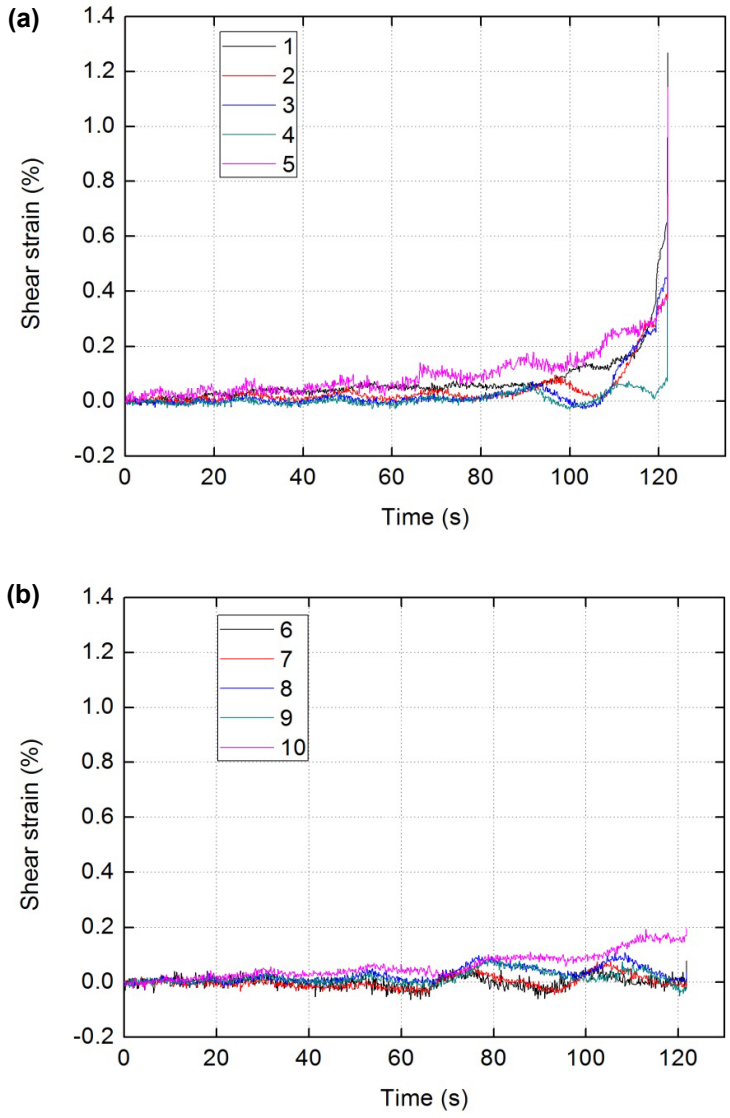

Figure 8. Variations of shear strain along (**a**) the mixed shear-tensile crack and (**b**) tensile crack.

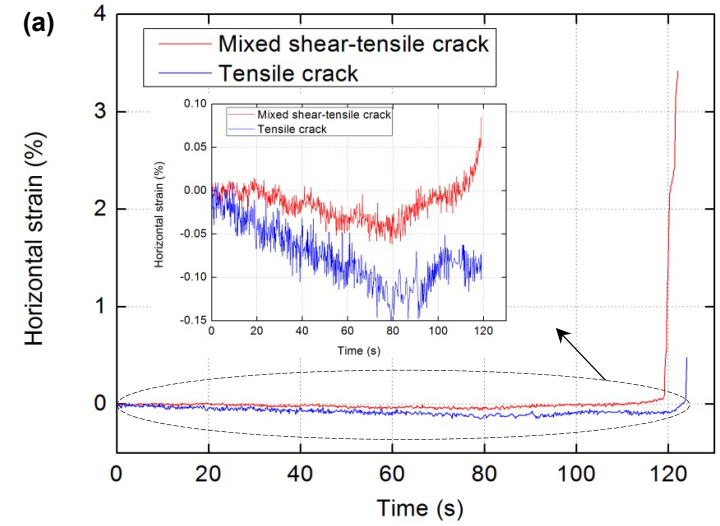
(a)
Mixed shear-tensile crack
Tensile crack
Horizontal strain (%)
Time (s)
Mixed shear-tensile crack
Tensile crack
Horizontal strain (%)
Time (s)

754

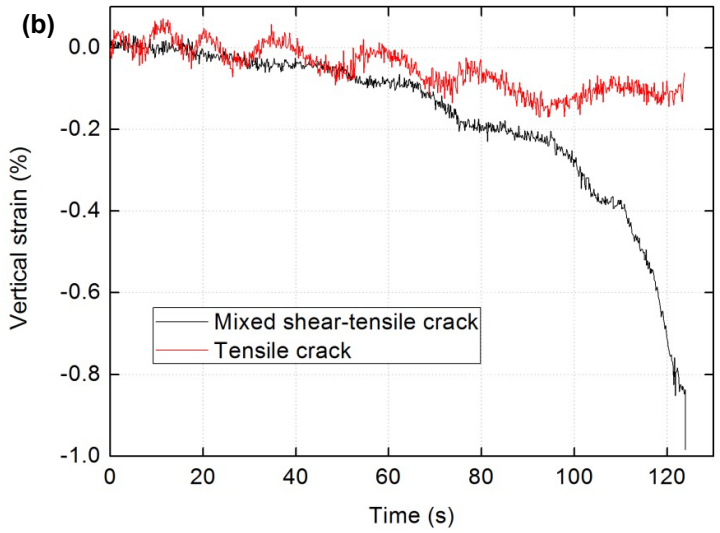
(b)
Vertical strain (%)
Mixed shear-tensile crack
Tensile crack
Time (s)

755

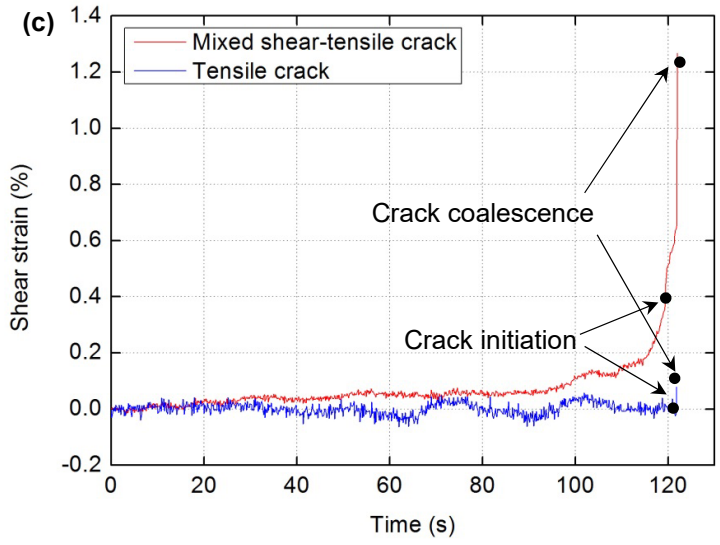
(c)
Mixed shear-tensile crack
Tensile crack
Shear strain (%)
Crack coalescence
Crack initiation
Time (s)

756

757 **Figure 9.** The variations of (**a**) horizontal strain, (**b**) vertical strain and (**c**) shear strain

758 of mixed shear-tensile crack and tensile crack in cracking process.

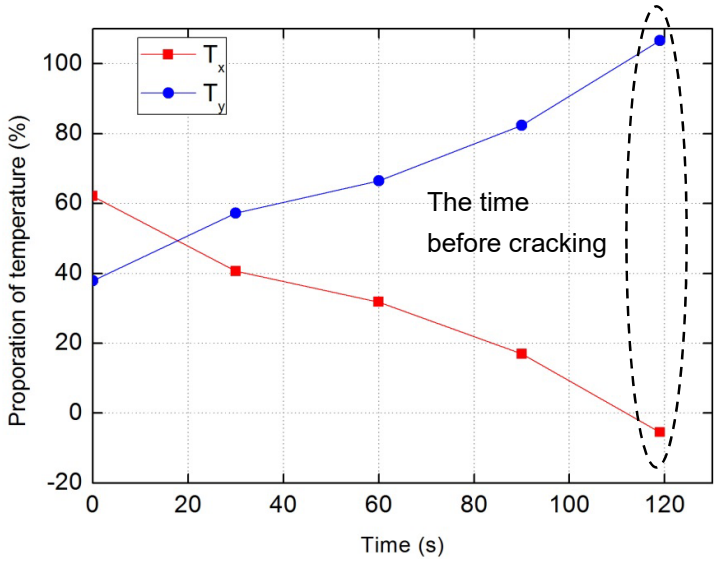

759

760 **Figure 10.** The proportion of temperature caused by σ_x and σ_y at initiation points for

761 the mixed shear-tensile crack.

762

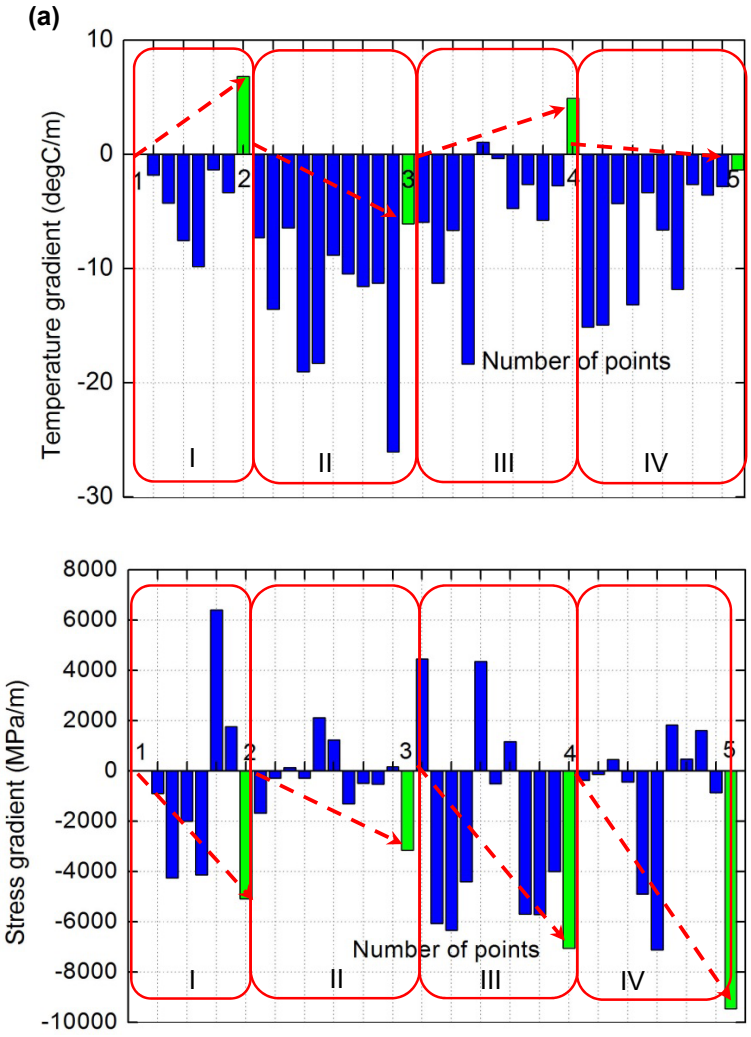
(a)
Temperature gradient (degC/m)
10
0
-10
-20
-30
1
2
3
4
5
I
II
III
IV
Number of points
Stress gradient (MPa/m)
8000
6000
4000
2000
0
-2000
-4000
-6000
-8000
-10000
1
2
3
4
5
I
II
III
IV
Number of points

763

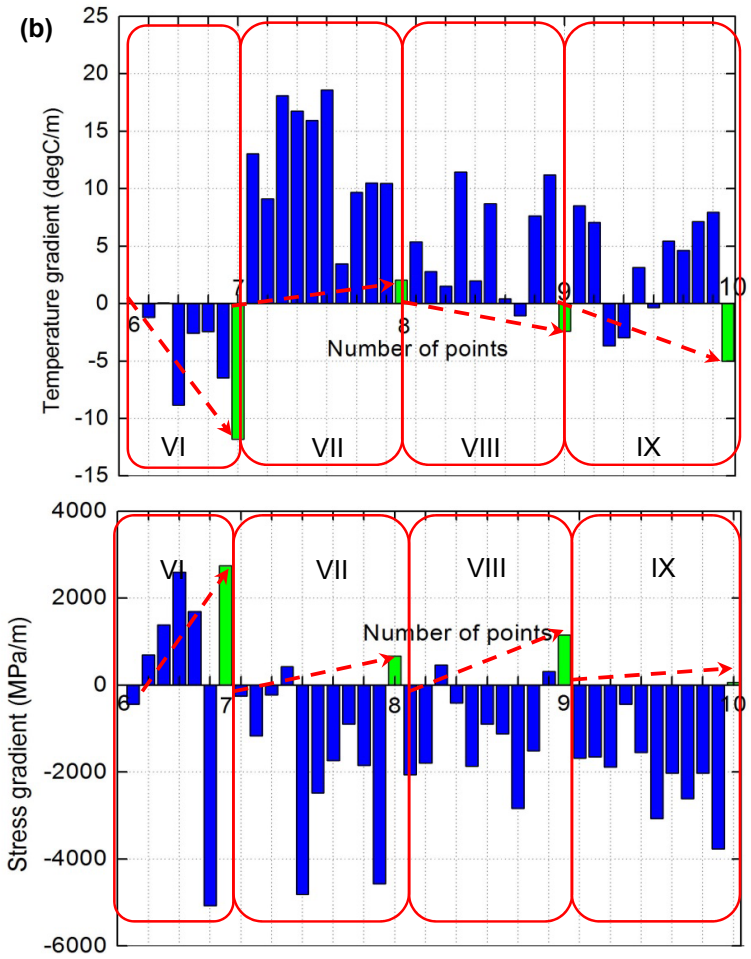

764

765 **Figure 11.** Comparisons between average temperature gradients and stress gradients

766 along the cracks, (**a**) the mixed shear-tensile crack, (**b**) tensile crack.

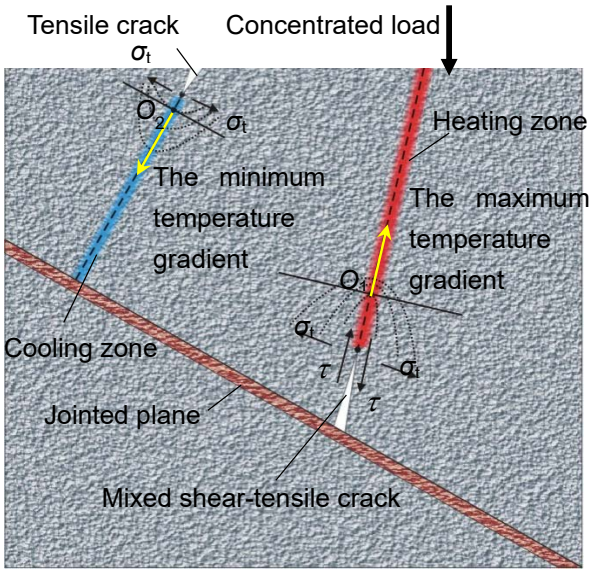

Figure 12. Temperature field along the cracks. Healing zone and cooling zone occur along the trajectories of the mixed shear-tensile crack and tensile crack, respectively.

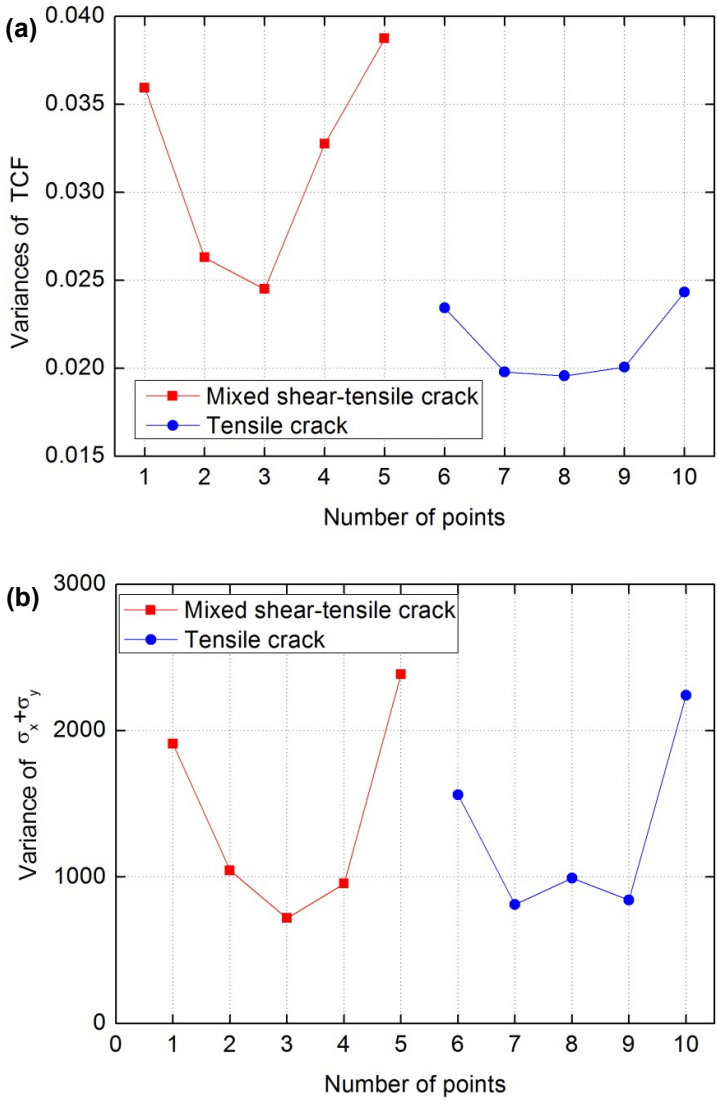

Figure 13. Comparisons between (**a**) variances of temperature concentration factor and (**b**) $\left(\sigma_x + \sigma_y\right)$ for the mixed shear-tensile crack and tensile crack.

786

787

788 **Table 1.** Physical and mechanical properties of granite and jointed plane

	ρ /g/cm^3	E /GPa	σ_c /MPa	σ_t /MPa	v	c /MPa	φ /
Granite	2.6	39.8	124.7	12.3	0.21	12.5	45.0
Joint plane	2.1	5.6	29.3	1.5	0.15	0.57	32.0

789

790